Chemical Geology 513 (2019) 108–119

Contents lists available at ScienceDirect

Chemical Geology

journal homepage: www.elsevier.com/locate/chemgeo

Improving confidence in ferromanganese crust age models: A composite geochemical approach

Pierre Josso[a,*], Ian Parkinson[b], Matthew Horstwood[a], Paul Lusty[a], Simon Chenery[a], Bramley Murton[c]

[a] British Geological Survey, Environmental Science Centre, Keyworth, Nottingham NG12 5GG, United Kingdom
[b] School of Earth Sciences, University of Bristol, Wills Memorial Building, Queens Road, Clifton BS8 1RJ, United Kingdom
[c] National Oceanography Centre, Waterfront Campus, European Way, Southampton SO14 3ZH, United Kingdom

ARTICLE INFO

Editor: B Kamber

Keywords:
Age model
Fe-Mn crust
Tropic seamount
Os isotopes
Co-chronometer
U-Pb LA-ICP-MS
Statistical modelling
Markov Chain Monte Carlo simulation

ABSTRACT

Accurate age models for marine ferromanganese (Fe-Mn) crusts are essential to understand paleoceanographic changes and variations in local environmental factors affecting crust growth rate and their lateral continuity. However, no absolute method exists for dating these deposits beyond the age of 10 Myr, which requires the combination of a number of approaches. Here, we present a composite age model for a 15 cm thick Fe-Mn crust sample obtained by unique core drilling using a remotely operated vehicle at a water depth of 1130 m, on the summit of Tropic Seamount, in the north-east Atlantic. The age model is based on cross-validation of laser-ablation U-Pb dating, Co-chronometry and Os isotopes. These enable robust calibration of the age-depth model using the Bayesian statistical modelling of Markov Chain Monte Carlo (MCMC) simulations. The results show that this Fe-Mn crust commenced growth in the Late Cretaceous between 73 and 77 Ma, and grew at a rate between 1 and 24 mm/Myr, averaging 4 mm/Myr. The phosphatised carbonate substrate, capping Tropic Seamount and underlying most of the Fe-Mn crusts, yields a U-Pb age of 84 ± 4 Myr, and provides the upper age limit for the model. Less radiogenic excursions of $^{188}Os/^{187}Os$ in the vertical profile through the crust permit the identification of key inflection points in the Os isotope seawater curve at the Eocene-Oligocene and Cretaceous-Paleogene transitions. Growth rates estimated from the empirical Co-chronometer are combined with the age envelope defined by the Os data and used to validate the MCMC simulations. The model identifies five hiatuses that occurred during the Pliocene (2.5 ± 1.9–5.3 ± 1.7 Ma), Early Miocene (16 ± 1–27 ± 2 Ma), Oligocene (29 ± 2–32 ± 1 Ma), Eocene (41 ± 2–52 ± 0.6 Ma), and the Late Paleocene (55 ± 1–59 ± 1.4 Ma). A major phosphatisation event affecting the Fe-Mn core can be dated to the Late Eocene (38 ± 1.2 Ma), which coincides with a recorded change in the global oceanic system, from warm and sluggish circulation to cold and vigorous thermohaline-driven meridional overturn at the onset of Antarctic glaciation.

1. Introduction

Ferromanganese (Fe-Mn) crusts are found in all oceans at depths between 400 and 7000 m beneath sea level (mbsl), where they accumulate on exposed hard rock substrates, such as the flanks and summit of seamounts, ridges and sediment-free plateaus (Josso et al., 2017; Koschinsky and Hein, 2017; Lusty et al., 2018). Formed directly from ambient seawater, these hydrogenetic encrustations accumulate very slowly (a few mm/Myr) through the precipitation of Fe and Mn oxyhydroxide colloids. The potential relative contribution of biogenic, biologically-induced or abiogenic processes to crust formation remains uncertain (Templeton et al., 2009; Wang and Müller, 2009). Their high specific surface area (mean 325 m^2/g), dipolar charge and long exposure-time to seawater, mean Fe-Mn oxyhydroxide particles are effective at scavenging dissolved trace elements (Hein et al., 2000). These properties, combined with surface-enhanced oxidation reactions that favour retention of redox-sensitive elements, make Fe-Mn crusts a net sink for many elemental species dissolved in seawater. Their processes of formation mean they represent condensed archives of the compositional evolution of seawater through time, recording climatic and geomorphological changes, such as periods of tropical weathering, glacial erosion and the opening and closing of pathways between

* Corresponding author.
E-mail address: piesso@bgs.ac.uk (P. Josso).

https://doi.org/10.1016/j.chemgeo.2019.03.003
Received 5 December 2018; Received in revised form 28 February 2019; Accepted 4 March 2019
Available online 07 March 2019
0009-2541/

oceanic basins, which influence global ocean chemical budgets.

Since their discovery, Fe-Mn crusts have been studied to reconstruct paleoceanographic conditions using Sr, Nd, Pb, and more recently Os and Hf isotopes with various degrees of success (Hein et al., 2000). There are several major challenges inherent to the use of Fe-Mn crusts for detailed, high-resolution paleoceanographic research. Their slow accumulation rate (averaging 1–10 mm/Myr), limits the temporal resolution of the conventional stratigraphic subsampling approach of micro-drilling, to time intervals of 50–500 Ka. Crust stratigraphy is also difficult to date with precision or accuracy. Their mineralogy and structure results in high porosity (mean of 60%, Hein et al. (2000)), which allows almost constant contact between ambient seawater and the internal layers of the deposit. This promotes equilibration of elements with a high post-depositional exchange rate with the contemporaneous ocean signature. This precludes the use of well-established geochronological methods such as absolute U-Pb dating, due to the diffusion of U into the Fe-Mn oxides (Claude et al., 2005; Goto et al., 2014; Henderson and Burton, 1999), or comparison of Sr isotopic signatures with the Sr seawater curve, as is routinely applied to marine carbonates (Futa et al., 1988; Ingram et al., 1990; Vonderhar et al., 1995). However, these methods can still be applied to the substrate or inclusions contained within Fe-Mn crusts to provide a constraint on the age of formation of the deposit. In contrast to carbonates, the relatively high concentration in crusts of elements of importance (Pb, Nd, Os, Hf) for paleoceanographic research means diagenetic isotopic exchange is not considered to be an important influence (Hein et al., 2000). It is therefore vital to establish a reliable and absolute chronology for Fe-Mn crusts, to correlate the isotopic and compositional changes in ocean chemistry, recorded by crusts, with identified climatic and paleoceanographic events (Claude et al., 2005).

Crusts can be accurately dated up to 1 Myr using ($^{230}Th)_{ex}$ and ($^{230}Th_{ex}/^{232}Th$) methods and up to 10 Myr using the $^{10}Be/^{9}Be$ chronology (Claude et al., 2005). Nanofossil biostratigraphy is another reliable dating method but has not been extensively used due to the difficulty in extracting and identifying the relatively sparse fossil tests from the Fe-Mn oxide layers. For the older portions of crusts, studies have extrapolated the average growth rate derived from $^{10}Be/^{9}Be$ chronology (Abouchami et al., 1999; Christensen et al., 1997; Frank and O'Nions, 1998; Lee et al., 1999; Ling et al., 1997; Reynolds et al., 1999), and used ages derived from so-called Co chronometer models. Two contemporaneous studies (Manheim and Lane-Bostwick, 1988; Puteanus and Halbach, 1988) explored the relationship between Co content and the accumulation rate of Fe-Mn deposits to establish an empirical equation for growth rate (GR in mm/Myr):

(Puteanus and Halbach, 1988)

$$GR = 1.28/([Co] - 0.24) \quad (1)$$

(Manheim and Lane-Bostwick, 1988)

$$GR = 0.68^{*}((([Fe] + [Mn])/(50^{*}[Co]))^{1.67}) \quad (2)$$

The method developed by Puteanus and Halbach (1988), is based on the assumption that the Co supply to the ocean is constant (Halbach et al., 1983) and that its incorporation into Fe-Mn crusts is purely hydrogenetic, with detrital contributions being negligible. By comparing the Co content of Fe-Mn crusts with ages obtained by radioactive decay profiles of $^{10}Be/^{9}Be$ and $^{230}Th_{ex}$, the authors derived empirical Eq. (1). Manheim and Lane-Bostwick (1988) took a similar approach, although they included data from a broader range of Fe-Mn oxide-bearing lithologies such as hydrothermal deposits and pelagic sediments to derive the growth rate relationship given in Eq. (2). As a result, the Manheim and Lane-Bostwick (1988) equation gives more extreme end-members and the resulting power regression may be a closer estimate of the growth rate of crusts. This has meant that their model is more widely used in the literature. Both methods assume a constant Co supply to the oceans and therefore the Co content of Fe-Mn crusts directly relates to the level of dilution caused by varying growth rates and the supply of detrital components. As such, crust ages derived from Co-chronometer models reflect minimum ages, as these techniques do not take account of growth hiatuses and erosive surfaces in the Fe-Mn deposits. Both methods have been independently employed to identify the minimum age of crust samples and calibrate isotopic and geochemical data in paleoceanographic reconstructions (David et al., 2001; Frank et al., 1999; Hu et al., 2012; Ling et al., 2005; Marino et al., 2017).

As a result of the limitations of the Co chronometer, two other methods have been considered for dating Fe-Mn crusts. In contrast to Sr, the rate of Os isotope diffusive re-equilibration is very slow and therefore has a negligible effect on Os isotope compositions over the time scales of Fe-Mn crust formation (Burton et al., 1999). Osmium has a residence time in seawater of a few thousand to 50 Ka. Hence, it can be used to develop age models by comparison with an independently determined and dated profile of seawater isotope ratio evolution through the Cenozoic (Burton et al., 1999; Klemm et al., 2005; Peucker-Ehrenbrink and Ravizza, 2012). Matching the Os isotope trend of subsamples taken from Fe-Mn crust with the seawater Os isotope curve allows age determinations to be made. The precision of the age is a direct function of the amplitude of isotopic variation preserved in the record. A second technique, magnetometer and SQUID analysis of Fe-Mn crusts layers, provides a very high-precision record of the magnetic reversals recorded by the Fe and Ti oxides in a crust (Joshima and Usui, 1998; Noguchi et al., 2017; Oda et al., 2016; Oda et al., 2011). This technique is the highest precision approach for determining the age of a crust, as the dates of magnetic reversals are well defined during the Cenozoic. However, due to the risk of hiatuses, this method needs to be combined with an absolute dating technique, such as ^{10}Be, U series, ($^{230}Th)_{ex}$ or Os isotopes, to allow the magnetic reversals to be correlated with the documented paleomagnetic record. In the absence of this, it is necessary to assume that the surface of the crust was growing until it was collected, and therefore provides the zero age reference point, and that the rest of the crust sample contains no hiatuses.

Here, we present the development of a composite age model for a 15 cm thick Fe-Mn crust sample collected from Tropic Seamount in the north-east Atlantic, during the JC142 expedition, which was part of the NERC-funded 'MarineE-tech' project. We examine current best-practice and the importance of using multiple techniques (LA-ICP-MS U-Pb dating, Os isotopes, and Co-chronometry) to cross-validate results and produce more robust age models for Fe-Mn crusts. A combination of proxies is optimised through Bayesian statistical modelling to produce a composite age-depth relationship with reduced uncertainty.

2. Geological background

Tropic Seamount is an isolated volcanic edifice in the northeast Atlantic. It forms part of the Western Saharan Seamount Province (WSSP) and is located 400 km from the passive continental margin of West Africa, halfway between the Canary Islands and Cape Verde Islands (Fig. 1A). The entire volcanic region initiated development in the early Cretaceous (e.g. the oldest known seamount being Bisabuelas at 140.5 ± 0.7 Myr), with activity continuing until present (El Hijo Seamount, 0.24 ± 0.02 Myr). The majority of volcanic activity was during the middle Miocene (Patriat and Labails, 2006; van den Bogaard, 2013). $^{40}Ar/^{39}Ar$ dating indicates that Tropic Seamount principally developed from eruptions in the late Aptian (119–114 Ma), with minor volcanic episodes occurring up until the middle Paleocene (60 Ma) (Schmincke and Graf, 2000; van den Bogaard, 2013). Tropic Seamount is emplaced on oceanic crust that is now 155 Myr old, based on the surrounding seafloor's paleomagnetic anomaly 'M25' (Blum et al., 1996) and hence it was only 35–40 Myr old when the formation of Tropic Seamount commenced.

Tropic Seamount rises from the abyssal plain at 4100 mbsl to a depth of 950 mbsl where it has a diamond-shaped flat summit (Fig. 1B). The flanks are dominated by gullies and landslide scars separated by four spurs radiating from the summit, exposing volcanic rocks,

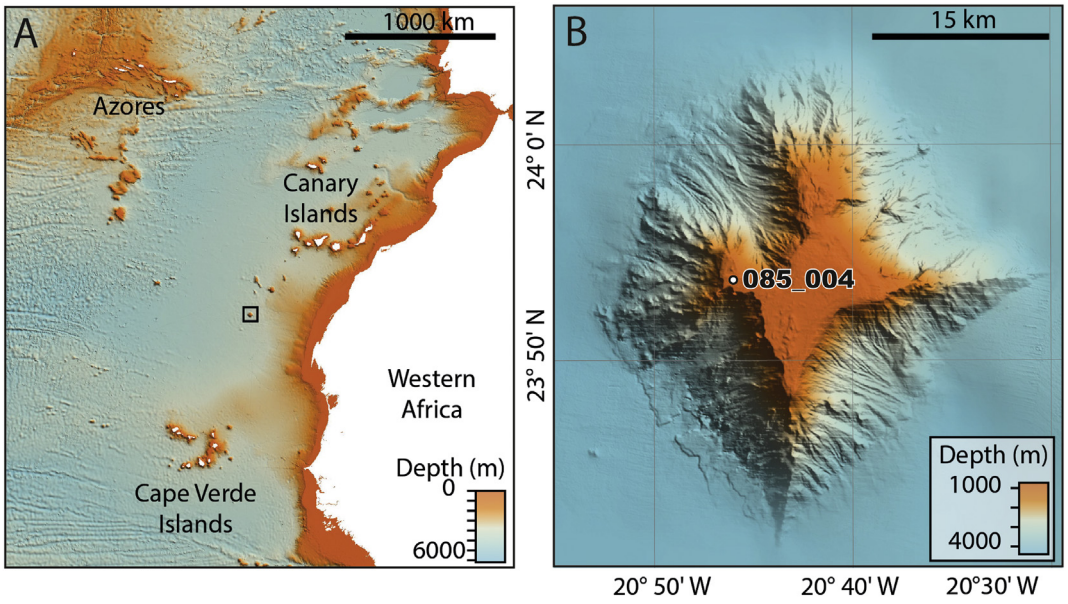

Fig. 1. (A) Regional setting of Tropic Seamount, NE Atlantic, located halfway between the Canary Islands and the Cape Verde islands (Bathymetry from GEBCO: Becker et al. (2009)). (B) Bathymetric map of Tropic Seamount obtained from the ship-based EM120 during JC142, gridded at 50 m and showing the location of core 085_004 (modified from Yeo et al. (2018)).

blanketed by loose sediments (Palomino et al., 2016). The summit plateau is covered by carbonate platforms encrusted with Fe-Mn oxides, unconsolidated pelagic ooze, and foraminiferal sand. This truncated morphology results from erosion by wave action, as is evident from the numerous terraces and raised beach features observed in high-resolution bathymetry and from remotely operated vehicle (ROV) images, and supported by the occurrence of conglomerates, dredged from the summit (Schmincke and Graf, 2000).

Ferromanganese crusts from Tropic Seamount were first investigated in the 1990s (SONNE expedition SO83) and then in 2011 (RV Miguel Oliver DRAGO0511) and most recently in 2016 (RRS James Cook JC142). Based on $^{10}Be/^{9}Be$ dating of a 38 mm thick crust sample, Koschinsky et al. (1996) determined an age of 12.3 Myr and an average growth rate of 3 mm/Myr. In contrast, using the Co chronometer model of Manheim and Lane-Bostwick (1988), Marino et al. (2017) and (2018) calculated bulk growth rates of 1.2–1.8 mm/Myr and growth rates of 0.54–0.9 mm/Myr using EMPA analysis of individual growth layers. These growth rates date the Fe-Mn crusts from Tropic Seamount at between 50 and 99 Ma.

3. Material and methods

3.1. Core material 085_004

Sample JC142_085_004, the primary focus of this study, was recovered on the western arm of the summit area of Tropic Seamount (Fig. 1B). The sample is a 20 cm long core acquired by drilling through a Fe-Mn crust pavement at a depth of 1130 mbsl with an ROV-mounted drill. The drilling recovered a 15 cm thick section of Fe-Mn crust overlying a phosphatised, biogenic debris-rich carbonate substrate (Fig. 2).

At a macroscopic scale, the core can be visually subdivided into three layers based on textural changes and detrital content. Layers 1 and 3 are black with massive textures and well-laminated oxide beds. Layer 2 comprises alternating zones of Fe-Mn oxide containing abundant brown detrital material and sub-millimetric columnar textures (Fig. 2). The top of layer 2 marks the end of the phosphatisation front in the sample (Supplementary information 5). In addition to these layers, four major erosive surfaces can be visually identified in layer 3 (E1 to E4, Fig. 2). The top of the sample has a polished texture resulting from the mechanical abrasion by sediment-laden currents, a feature commonly observed on Tropic Seamount (Lusty et al., 2018). A discordant contact occurs between 2 and 6 mm from the top of the core, cutting obliquely across the Fe-Mn oxide layers, indicating that at least 4 mm of crust has been locally eroded. In the subsequent discussion, all depths quoted relate to the top of the core sample, i.e. 0 mm. The third erosive surface is defined by an undulating discordant contact, located above nodular calcite masses between 40 and 45 mm (Fig. 2) that was identified in thin section with an optical microscope. The final discontinuity that is visually apparent in the core is located at a depth of 51 mm, where the core has broken during the drilling process. Carbonate veins are abundant in layer 3 and these follow stratigraphic discontinuities between the layers. Phosphatised carbonate veins occur between 139 and 148 mm, cross-cutting the oxide layering.

3.2. Core preparation

The core was split and half was fully impregnated with epoxy resin under vacuum conditions. This was then cut into three pieces, with the cut direction oblique to the layering, to ensure stratigraphic continuity between the three polished thin sections subsequently produced from the blocks.

3.3. Subsampling for ICP-MS analysis and Os isotopes

The second half of the core was subsampled using a hand-held microdrill to obtain samples along a profile perpendicular to the layering with a spatial resolution of 500 µm. 123 Fe-Mn crust subsamples were taken from individual growth layers across the width of the core, each averaging 20 mg of material after drying.

3.4. ICP-MS

Whole-rock geochemistry was obtained from the 123 micro-drilled subsamples for calculation of the Co-chronometers. While it is true Co-chronometers have been designed to use the hydrogenous component for Co, it has been demonstrated by numerous sequential leaching experiments, notably by Koschinsky and Halbach (1995) and Koschinsky and Hein (2003), that 99% of the total Co content of various Fe-Mn crusts samples is hosted by the hydrogenous Fe-Mn oxides, while the

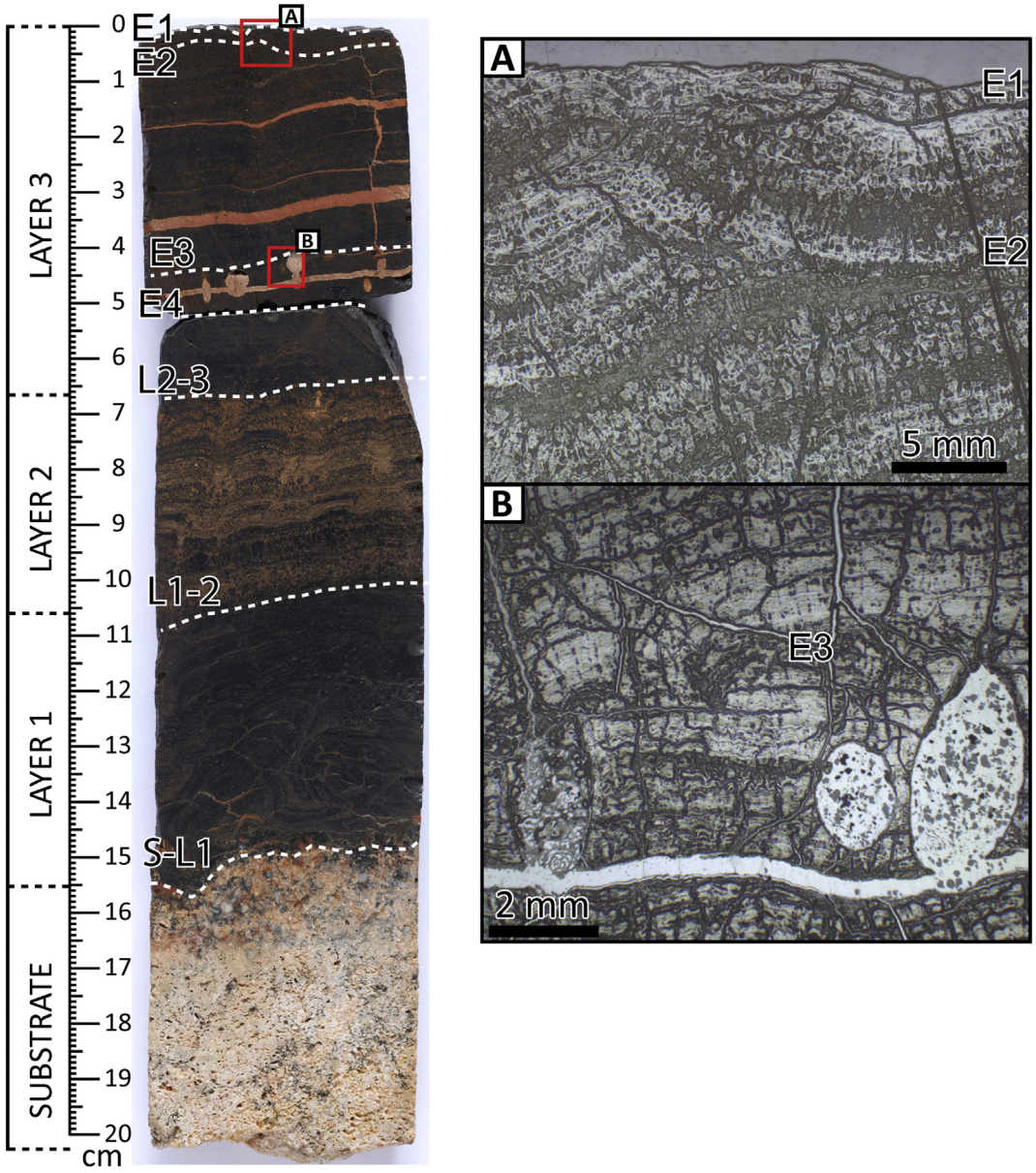

Fig. 2. Cut section of core sample 085_004, which shows three visually distinct layers of Fe-Mn crust, containing a series of erosive surfaces (E1–4), overlying a light coloured, biogenic-rich phosphatised carbonate substrate. Panels A and B are microphotograph of the erosive surface E1, E2, and E3, highlighted by the discordant contact of Fe-Mn oxide layers on each side of the surface.

residual phases have very little if no Co at all. Therefore, whole-rock geochemistry provides an excellent approximation of the hydrogenous Co content, which would not be distinguishable within analytical uncertainty from leachable Co. Samples were first digested overnight in closed HDPE vessels at 80 °C using a mixture of 1 ml 5% HNO_3, 1 ml 50% HNO_3 and 2 ml 50% HCl at the British Geological Survey (BGS). Following dry down, 2 ml of concentrated HNO_3, 0.5 ml HF and 0.1 ml $HClO_4$ were introduced and allowed to react in open vessels up to a temperature of 130 °C over 18 h, then cooled down to 50 °C. Dry residues were redigested with 1 ml 50% HNO_3 and HCl for 30 min and a mixture of MQ and H_2O_2 was added before transfer to HDPE bottles for storage. All reagents used were analytical grade. Following the complete acid digestion, whole rock geochemical analysis was conducted by inductively coupled plasma mass spectrometry using an Agilent Technologies 8900 ICP-MS Triple Quadrupole. Major, minor and trace elements were analysed for each subsample. Here, we only report data for Fe, Mn, P, and Co because of their use in Co-chronometry calculation. The other geochemical data for core 085_004 is not presented here. Certified reference materials (CRM) NodA-1, NodP-1, JMn-1 and a homemade reference material (HRM) derived from a Tropic Seamount sample, were used to assess repeatability and to monitor drift; these were analysed in triplicate following identical sample preparation and digestion procedures. The analyses on the CRM's demonstrate accurate results on average (± 10–15%, 2σ) but the amount of material sampled (0.008–0.02 g) was less than that for which the reference values were determined by fusion bead (0.3 g). As a result, the heterogeneity of each CRM biased the individual preparations around the mean. Reproducibility on the HRM, that was ground to a much finer grain size during preparation at BGS laboratories, demonstrates better reproducibility with $2\sigma < 5\%$ for P, Fe, and Co whilst Mn reproducibility was at 6.9% (2σ), consistent with artificial QC solutions ($n = 7$) giving $2\sigma < 5\%$ for P, Mn, and Fe whilst Co reproducibility was 8%.

3.5. Os isotopes measurements

A further 53 micro-drilled sub-samples were recovered from various

stratigraphic horizons in the core for Re−Os isotope analysis. Osmium isotopes and Os and Re concentrations were determined at the School of Earth Sciences, University of Bristol. Samples were digested in Carius tubes using techniques modified from Shirey and Walker (1995). 0.012 to 0.090 g of powder was added to the Carius tubes along with 8 ml of inverse aqua regia and ^{190}Os and ^{185}Re spikes. The samples were digested at 230 °C for 48 h. This technique recovers hydrogenic Os and Re without dissolving any detrital material. However, some samples yielded very low Re concentrations, so three samples were fully dissolved using HF, HNO_3, and HCl to determine the Re concentrations. Two samples yielded low Re concentrations consistent with the Carius tube digestions, suggesting many of the samples truly contained little Re. One sample did have higher Re concentrations following the full digestion and verifies that the dissolution technique extracts the hydrogenic component, without incorporating detrital silicate material, derived from the proximal western African craton (e.g. Saharan dust or other weathering products).

Osmium and Re were separated using solvent extraction techniques, with Os back-extracted from the inverse aqua-regia into CCl_4 and then into HBr (Cohen and Waters, 1996), before final purification by microdistillation (Birck et al., 1997). Rhenium was purified by drying down the inverse aqua regia, taking up in 2N HNO_3 and back-extracted into isoamylol (3-methyl-1-butanol). The isoamylol was cleaned with 2N HNO_3 and the Re back extracted into MQ H_2O before being dried (Birck et al., 1997) and finally taken up in 2% HNO_3 for analyses.

For the Os isotope analyses, the samples were loaded in HBr on zone-refined Pt filaments, and a $Ba(OH)_2$/NaOH activator was added to the sample. Osmium isotopes were analysed as OsO_3^- ions using a secondary electron multiplier (SEM) on a ThermoFisher Triton thermal ionisation mass spectrometer (TIMS) in N-TIMS mode. Data were corrected for minor oxygen isotope interferences and any isobaric Re interference, with instrumental mass fractionation corrected for using the exponential mass fractionation law and a ^{192}Os/^{188}Os ratio of 3.08271. Osmium concentrations were determined by isotope dilution and the isotope data was spike-stripped to yield the sample ^{187}Os/^{188}Os ratio. Total procedural blanks were determined for each dissolution batch and yielded Os concentrations of 0.3 ± 0.1 pg with a ^{187}Os/^{188}Os ratio of 0.1784. All data were corrected for the procedural blank with blank corrections usually < 2% (range 0.4 to 7.7%) on the concentration and usually < 0.8% (range 0.063–2.46%) on the ^{187}Os/^{188}Os ratio depending on sample size and Os concentration. A DTM (Department of Terrestrial Magnetism) solution standard was analysed during the analytical period and yielded a ^{187}Os/^{188}Os ratio of 0.173966 ± 386 (2σ, n = 12), within the error of previous determinations of the standard (e.g. Birck et al. (1997)). Precision on the standard is 2.22‰, whereas 2σ precision on the samples is generally 2–6‰ due to the small amounts of Os loaded on to the filament and these uncertainties are given in the Supplementary data 1.

Rhenium isotopes were measured by multi-collector inductively plasma source mass spectrometry (MC-ICP-MS) on a ThermoFisher Neptune using an SEM. A 2% HNO_3 on-mass blank was measured before each sample and both on-mass blank and samples were doped with 20 ppb Ir with ^{191}Ir and ^{193}Ir, which were measured on the Faraday cups. The ^{185}Re and ^{187}Re intensities for each sample were corrected with the on-mass blank and each sample was then corrected for instrumental mass fractionation using the exponential mass fractionation law and a ^{191}Ir/^{193}Ir ratio of 0.59418. Total procedural blanks were determined for each dissolution batch and yielded Re concentrations of 1.53 to 5.13 pg, with Re concentrations determined by isotope dilution and blank corrected using the appropriate procedural blank. Many samples had low Re concentrations; some had concentrations above the detection limit of the MC-ICP-MS (i.e. had positive counts after on-mass corrections) but were within error of zero after blank correction whereas some samples yielded ^{187}Re counts below the 2% HNO_3 acid blank. Rhenium blank correction was substantial for many samples (> 10%) and 2σ uncertainties on samples range from 4 to 27‰ depending on sample size. A 9 ppt solution of the NIST SRM3134 Re standard, doped with Ir, was run during the analytical period and yielded a ^{187}Re/^{185}Re ratio within error of previous determinations of the standard (Miller et al., 2009).

3.6. LA-ICP-MS U-Pb dating

U-Pb dating of the carbonate basement and the phosphorite veins were undertaken by LA-ICP-MS using a Nu Instruments Attom single collector sector field (SC-SF-ICP-MS) and an ESI (New Wave Research Division) NWR193UC excimer laser at the NERC Isotope Geosciences Laboratory (NIGL) of BGS (Supplementary Data 2 for operating conditions). Laser conditions and spot sizes varied depending on the U and Pb concentration of the reference materials and phosphatised portion of the ferromanganese crust. Data were normalised to the WC1 carbonate reference material (Roberts et al., 2017) and validated (in the case of the phosphorite vein sample) using Durango apatite, assuming a U-Pb age of 31.44 ± 0.18 Myr (McDowell et al., 2009). Laser operating conditions were 5–10 Hz, 3.25 J.cm^{-2} using a 50–75 µm spot size. Variation of spot size and repetition rate had no effect on the U-Pb normalisation as both conditions were represented in the same validation data. A 1 s pre-ablation run was completed prior to the 30 s ablation analysis to ensure cleanliness of the ablated surfaces. Data were collected in a time-resolved manner using the instrument software. U-Pb data normalisation and uncertainty propagation were done using an in-house Excel spreadsheet utilising WC1 as the primary reference material (calibration uncertainty 0.77%, 2σ, MSWD = 1.4, n = 24) and the Durango apatite standard as validation. Without further normalisation for carbonate versus apatite matrix effects, we obtain an age of 31.4 ± 1.3 Myr (2σ, MSWD = 2.0, n = 19) for the Durango apatite demonstrating the accuracy of the approach. The calculated ages and isochron plots were produced using Isoplot v.4.15 (Ludwig, 2012).

3.7. Age-depth modelling

Os isotopes, Co-chronometry and U-Pb dating were used to create an age model employing Bayesian statistical modelling (Blaauw and Christen, 2011). Using the “rBacon” package and “Bacon” function developed for R©, these three datasets are used in the model to define the age, accumulation rate, and valid gateway dates derived from Os isotope ratios, for the simulation of over 70 million MCMC iterations. The density of the resulting simulations defines an age-depth model reported as a mean with a 95% confidence interval. As the Bacon function was initially developed for calibration of ^{14}C-dated cores, internal calibration curves were disabled to ensure dates used in the model matched the Os isotope constraints (see Supplementary data 3 for detailed code).

4. Results

4.1. Laser-ablation U-Pb dating

In total, 60 measurements were taken from different parts of the phosphatised carbonate substrate, yielding an age of 84.0 ± 4.0 Myr (2σ, MSWD = 1.3, n = 60). All measurements for the validation material and sample are presented in Supplementary data 4. These results are much younger than the ages determined for the volcanic basement (119 Myr) (Fig. 3) and their difference is attributed to the period taken for the volcanic island to have been eroded and subside below sea-level. Therefore, the date for the carbonate substrate represents the maximum potential age of the initial deposition of Fe-Mn crust in this sample.

Diagenetic phosphorite veins crosscutting the basal Fe-Mn oxide layers between 139 and 148 mm were also analysed and give an age of 46 ± 10 Myr (2σ, MSWD = 0.82, n = 20). The higher uncertainty in these measurements marks the combination of initial low U content and

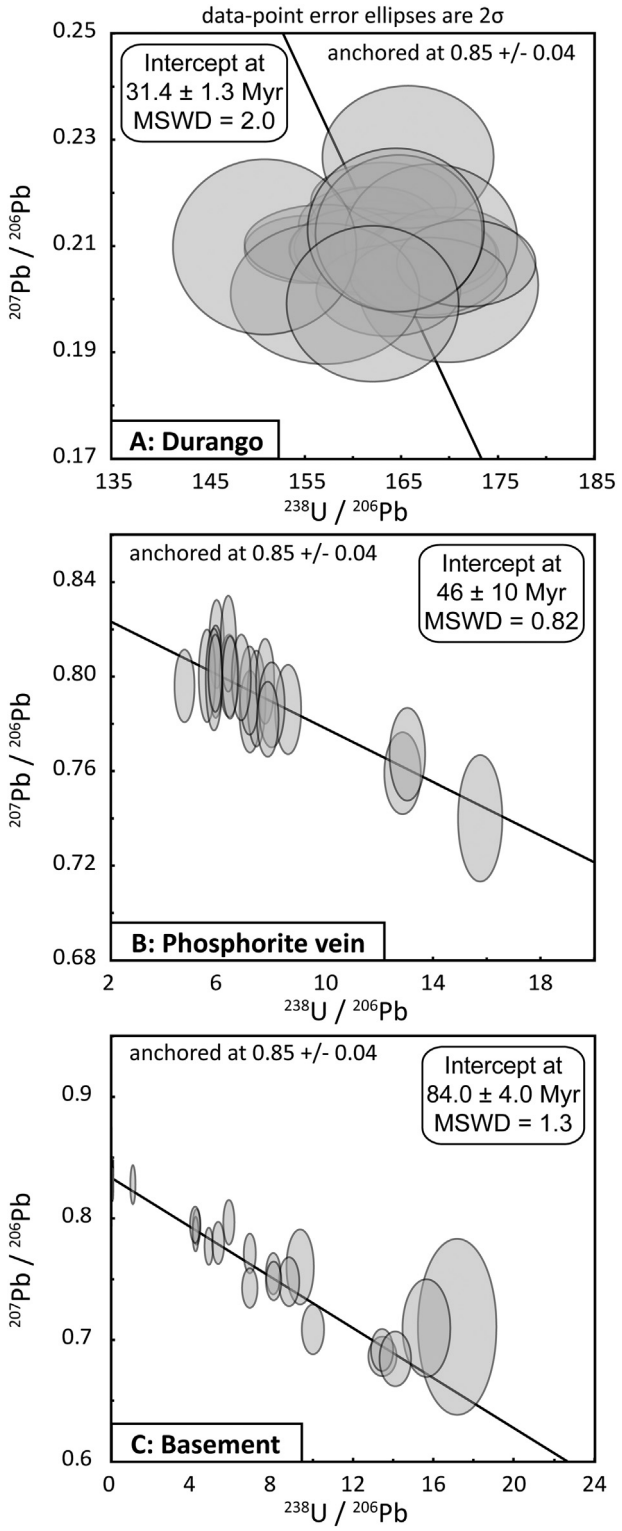

Fig. 3. U-Pb concordia diagram for (A) Durango apatite, (B) the phosphorite veins at the base of the core and (C) the phosphatised carbonate basement.

a low ratio of radiogenic/common Pb. This results in low $^{238}U/^{206}Pb$ - high $^{207}Pb/^{206}Pb$ data array and therefore the long projection of the Discordia regression to the Tera-Wasserburg Concordia curve. Similarly, laser ablation was conducted on the intercolumnar carbonate-fluorapatite (CFA, Fig. 2: layer 2) and calcite veins that occur close to the top of the sample (Fig. 2: layer 3). However, U concentrations were insufficient to determine an age.

These results provide an initial absolute age constraint on the Fe-Mn crust, as the crust hosting the vein must predate it, (e.g. be at least 36 Myr old), but its age cannot exceed that of its substrate. Accordingly, this sample of Fe-Mn crust started accumulating between 46 ± 10 Ma and 84 ± 4 Ma. Although these dates only limit deposition to a ~50 Myr window, they are valuable for constraining the results derived from the other techniques.

4.2. Co-chronometry

The results of the derived-age calculations from the 123 Fe-Mn crust subsamples using both the Manheim and Lane-Bostwick (1988) and Puteanus and Halbach (1988) models are presented in Fig. 4. The supporting data and calculations are described in Supplementary data 5. Due to the intense phosphatisation that occurs halfway down the core (69 mm, Supplementary data 5), the model from Puteanus and Halbach (1988) was calculated with the proposed correction for Co, Fe and Mn dilution by phosphatic phases. No correction for the effect of phosphatisation is proposed in the model of Manheim and Lane-Bostwick (1988), as [Co] in growth rate calculations (Eq. (1)) is directly proportional to [Fe] and [Mn]. However, it has been demonstrated that these two elements, although diluted by the addition of CFA in the system, are not similarly affected during phosphatisation episodes, which affects the assumptions associated with the proportionality between Co and the Fe and Mn content (Koschinsky et al., 1997). Uncertainties on growth rate estimates were calculated using quadratic addition of the 2σ uncertainty of each measurement for Mn, Fe, Co and P from the ICP-MS analysis (Supplementary data 5). Unsampled crust sections were accounted for in the Co-chronometer age model presented in Fig. 4, by linearly interpolating the growth rate from bracketing subsamples.

In the upper 70 mm of the core the two models positively co-vary with depth, but then diverge in the phosphatised portion of the crust. More importantly, the models yield a 3-fold difference in the resulting average growth rate and estimated age of the base of the crust, ranging from 39–45 Myr to 122–145 Myr (Fig. 4). Given that the age model based on Manheim and Lane-Bostwick (1988) yields an age for initiation of crust growth that is older than the carbonate substrate and seamount, it is clearly incorrect.

Based on the age derived from the Puteanus and Halbach (1988) model, sample 085_004 records a period of at least 39–45 Myr of Fe-Mn oxide accumulation. In this model, the growth rate oscillates between 1.7 and 5.0 mm/Myr in the unphosphatised portion of the crust (down to 69 mm) with an average growth rate of 3.4 ± 1.1 (2σ) mm/Myr. These results are consistent with the $^{10}Be/^{9}Be$ growth rate estimate of 3 mm/Myr reported by Koschinsky et al. (1996). Between 70 and 103 mm, the abundant detrital material and phosphates dilute the primary Fe-Mn oxide components resulting in a higher average growth rate of 6.2 ± 4.9 (2σ) mm/Myr, with localised growth rates as high as 24 mm/Myr (Fig. 4). These rapid growth rates result from the corrected Co value approaching 0.24 wt% (See Eq. (1)), in layers of the brownish material from Layer 2, and therefore represent the limit of the model's validity. Below 103 mm, the growth rate is relatively constant with an average of 3.0 ± 1.0 (2σ) mm/Myr.

The phosphorite vein, dated at 46 ± 10 (2σ) Myr, cross-cuts the section of Fe-Mn crust anticipated to be 39 Myr old based on Co-chronometry at 135 mm (Fig. 4). The Co-chronometer age is therefore within the uncertainty of the U-Pb measurements and no hiatuses could be identified with confidence based on these two proxies.

4.3. Os isotopes

$^{187}Os/^{188}Os$, Os, and Re concentrations were measured in 53 samples. The total Os concentrations range from 0.1 to 1.85 ppb with minimal concentrations in heavily phosphatised samples (70–110 mm) as a direct outcome of dilution by additional carbonate fluorapatite.

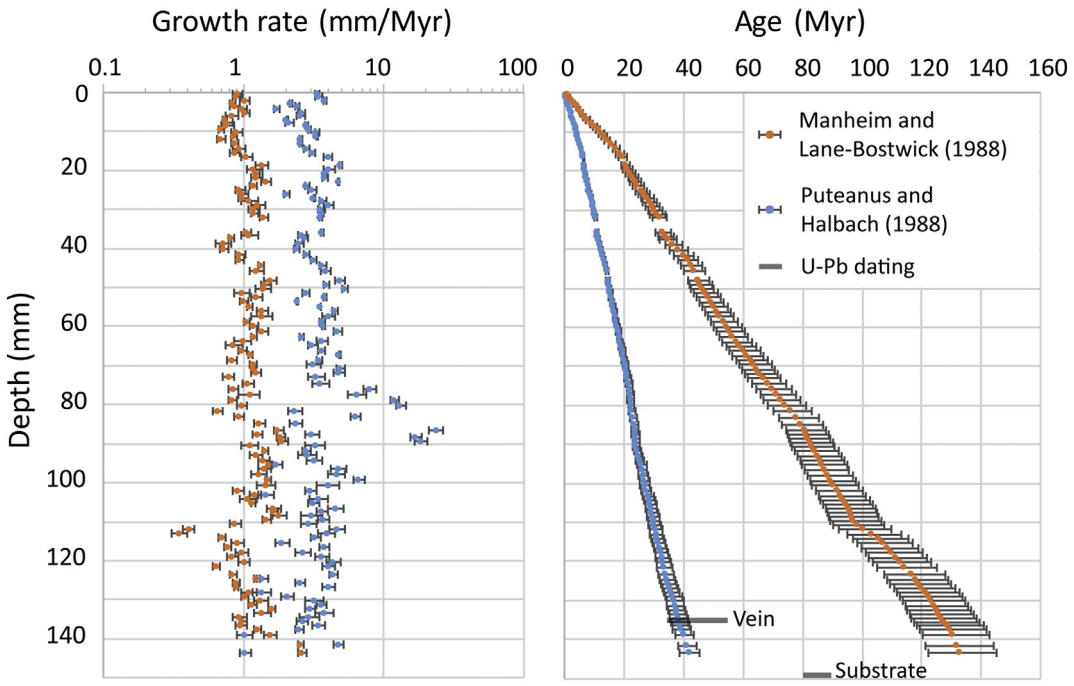

Fig. 4. (A) Growth rate calculations for all Fe-Mn crust subsamples and (B) reciprocal age-depth model derived from Co-chronometry equations of Manheim and Lane-Bostwick (1988) and Puteanus and Halbach (1988). Ages for the vein and substrate obtained from LA-ICP-MS U-Pb dating are also shown.

The Re content oscillates between concentrations below the detection limit and 576 ppt. Correction of ^{187}Os to account for ^{187}Re decay after crust formation was calculated for most samples (Supplementary data 1). Although there is a maximum potential ingrowth duration of 84 ± 4 Myr, $^{187}Re/^{188}Os$ ratios are largely between 0 and 1 (but up to 13.5), and as ^{187}Re has a half-life close to 41.2 Ga, the radiogenic ingrowth corrections have minor effects on the $^{187}Os/^{188}Os$ ratios (Supplementary Data 1).

The corrected ratios of $^{187}Os/^{188}Os$ vary from 0.93 to 0.30, with a smooth pattern showing the presence of three unradiogenic excursions (Fig. 5B). $^{187}Os/^{188}Os$ has erratic behaviour in the lowest part of the crust, grouped around values of 0.62. One very radiogenic sample by comparison (0.80) is difficult to position in the context of the overall trend. A radiogenic signature such as this could be the result of the inclusion of material derived from the proximal western African craton. However, the Carius tube digestion using inverse aqua regia should have prevented any contamination by non-hydrogenetic material as demonstrated by the comparison with a full acid digest (see methods). An alternative explanation is that the seawater Os isotope signature is too poorly known at the resolution required to confidently rule out this unradiogenic signature as a true seawater value, which has not previously been reported. The Os data then continuously decrease to unradiogenic values of 0.3 at a depth of 107 mm. Following this trough in the pattern, the Os ratios increase and plateau at values of 0.5 with the exception of one sample with a more unradiogenic Os isotopic composition at 89 mm, which clearly stands out from the well-defined stratigraphic interval, with $^{187}Os/^{188}Os$ ratios > 0.5. Abrupt unradiogenic excursions have been observed in Fe-Mn crusts where fragments of micrometeorite are incorporated in the deposit (Conrad et al., 2017). However, these extra-terrestrial materials have high PGE content and this subsample has some of the lowest Re and Os concentrations in the dataset. The effect of micro-meteorite contamination on our record is considered negligible. For example, only samples at 107 and 132 mm display positive concentration anomalies whilst showing minor negative isotopic excursions. However, 1/Os vs $^{187}Os/^{188}Os$ plots do not indicate any meteoritic influence. In general, the record does not show any mixing relationship. The only trend discernible in our dataset appears when isolating the six samples running up to the unradiogenic excursion at 54.5 mm, which introduce deliberate sampling bias. However, the trend is weak and corresponds to the smooth change in the seawater pattern. By contrast, the sample at 113.6 mm has a high Os content and more radiogenic signature than the surrounding samples. Extra-terrestrial material may cause some scatter in the data, but its influence will be minimised by our digestion method, and therefore is negligible given the approximation of the Os envelope, owing to the low data density in the literature. Therefore, we consider the measurement at 89 mm to represent a genuine record of seawater composition. The Os ratios then continuously increase to 0.6 over a distance of 30 mm before plunging steeply to unradiogenic values of 0.37 at 55 mm. After this trough, Os ratios rise in a step-wise manner up to the surface of the core, reaching $^{187}Os/^{188}Os$ of 0.92, slightly less radiogenic than the present day seawater value of ~1.08 (Peucker-Ehrenbrink and Ravizza, 2012).

The age model constructed here is based on Os isotope data and follows a probabilistic approach. As the data compilation of $^{187}Os/^{188}Os$ seawater ratios over the Cenozoic and Late Cretaceous (Fig. 5A) (Klemm et al., 2005; Pegram and Turekian, 1999; Peucker-Ehrenbrink and Ravizza, 2012; Ravizza and Peucker-Ehrenbrink, 2003; Reusch et al., 1998) lacks the temporal resolution for a precise, continuous record, due to Os residence time in seawater, an envelope was constructed based on an approximation of the average Os isotopic composition of seawater at a given time. As a result, one $^{187}Os/^{188}Os$ data point can fit many positions within the envelope and additional data is required to improve the $^{187}Os/^{188}Os$ seawater record. We consequently mapped all the potential ages that each sample could occupy within the seawater envelope. These age intervals are represented by the horizontal lines for each depth on Fig. 5C. Following simple stratigraphic principles (for instance, a sample cannot be older than the sample stratigraphically below it), an age envelope was constructed by connecting or intersecting those intervals that match the Os seawater curve. This iterative process progressively reduces the uncertainty, or spread of the envelope, as the constraints imposed by a single sample reduce the number of potential age intervals that samples located adjacent to it can represent. Whilst this is very similar to a best-fit approach between two trends of data, rather than arbitrarily positioning the sample within the seawater curve, the age envelope preserves a

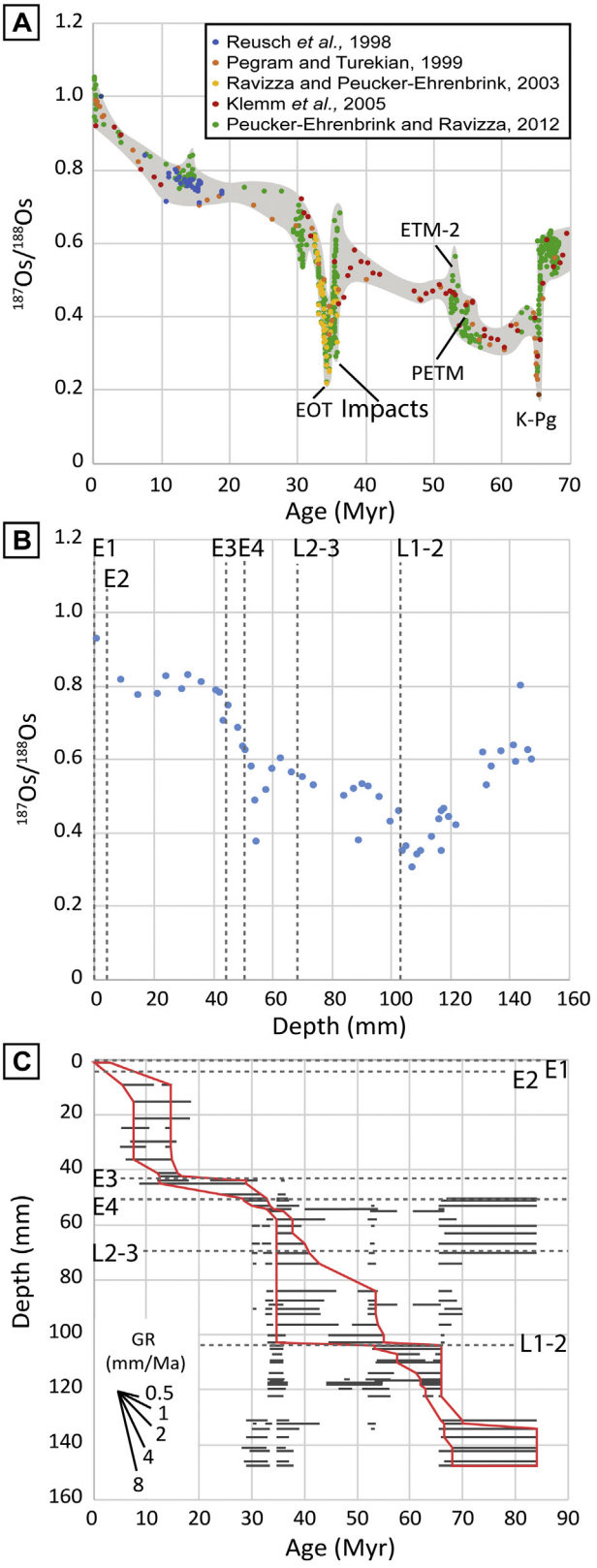

Fig. 5. (A) Compilation of Os isotope data from Reusch et al. (1998), Pegram and Turekian (1999), Ravizza and Peucker-Ehrenbrink (2003), Klemm et al. (2005), Peucker-Ehrenbrink and Ravizza (2012), defining the seawater $^{187}Os/^{188}Os$ evolution over the Cenozoic and Late Cretaceous. (B) $^{187}Os/^{188}Os$ vs. depth in core 085_004 with hiatuses and macro layers boundaries identified in Fig. 2. Note that the uncertainty of the $^{187}Os/^{188}Os$ data is smaller than the symbol. (C) Age vs. depth graph presenting all the potential ages a single $^{187}Os/^{188}Os$ data point may represent when plotted on the Os isotope seawater curve. Following simple stratigraphic relationships, an age envelope (in red) can be determined for the core. (For interpretation of the references to colour in this figure legend, the reader is referred to the web version of this article.)

degree of uncertainty that the Os isotopes data cannot resolve independently. As such, this envelope defines all the potential ages that each Os measurement can represent for a given stratigraphic interval, and the age intervals within it are used as a constraint on the numerical modelling described later.

The preservation in the seawater record of high-amplitude isotopic variation at the Eocene-Oligocene transition (EOT), Eocene thermal maximum 2 (ETM-2), Paleocene-Eocene thermal maximum (PETM) and Cretaceous-Paleogene (K-Pg) boundary is important for creating tie points in the age envelope. In contrast, periods of minimal isotopic variation, notably in the late Oligocene-early Miocene (30–10 Ma) and middle to late Eocene (50–38 Ma), result in a less well-constrained age model. This approach differs from the one adopted by Klemm et al. (2005) who applied the growth rate calculated from the Co-chronometer to their Os data from crust CD29, and therefore fixed this variable, implementing hiatuses in an arbitrary manner where the Co-chronometer-fitted-Os data did not match the seawater curve. Such an approach biases the age model by suppressing any information on the growth rate that is derived from the Os data and may differ from the Co-chronometer estimates. Whilst the precision of the Co-chronometers is debatable, the age envelope formed by the Os data is reliable and coherence between the methods should be sought. As such, growth rate estimates from Co-models should be validated against Os data rather than vice versa, to prevent circularity in the age estimates. The Os age model for crust CD29 was later revaluated (Nielsen et al., 2009) using distinctive points in the Os record to anchor the age model at the K-Pg and EOT transition and then extrapolating the age of other subsamples using linear interpolation. While less arbitrary, this method still assumes constant growth rates between each tie point and an absence of hiatuses, with the exception of when the distribution varies from the seawater Os record. As a result, it does not consider uncertainty in the age estimates.

The Os isotope data presented in this study allows the unradiogenic excursion at a depth of 55 mm ($^{187}Os/^{188}Os = 0.37$) to be identified as the EOT, whilst the transition from unradiogenic to radiogenic values at the bottom of the core highlights that the base of the crust is as old as Late Cretaceous. Unfortunately, an absence of more unradiogenic values ($^{187}Os/^{188}Os < 0.3$) in this interval does not permit the positioning of the K-Pg boundary with confidence. Whilst additional analyses, focusing on this stratigraphic interval may reveal such values, it is also possible that this time interval represents a growth hiatus and/or has been eroded.

4.4. Statistical modelling of the combined proxies

At this stage, each proxy has delivered independent chronological information on the stratigraphy of this Fe-Mn crust sample. Empirical growth rate calculations (1–24 mm/Myr, averaging 4 mm/Myr) suggest this crust sample represents at least 39–45 Myr worth of oxide accumulation, although this is a minimal as hiatuses and erosive surfaces are not accounted for by Co-chronometer age models. However, clear major unradiogenic Os isotope excursions indicate that the lower portion of the core extends beyond the K-Pg boundary. Interpretation of the older Os data is inherently limited by the Os record reported in the literature only extending back to ~70 Ma, as data for the Cretaceous are sparse. However, U-Pb dating of the carbonate basement at 84 ± 4 Ma, provides the maximum age limit for this deposit as the age of the crust cannot exceed its substrate.

While the methodology and accuracy of age-depth models derived

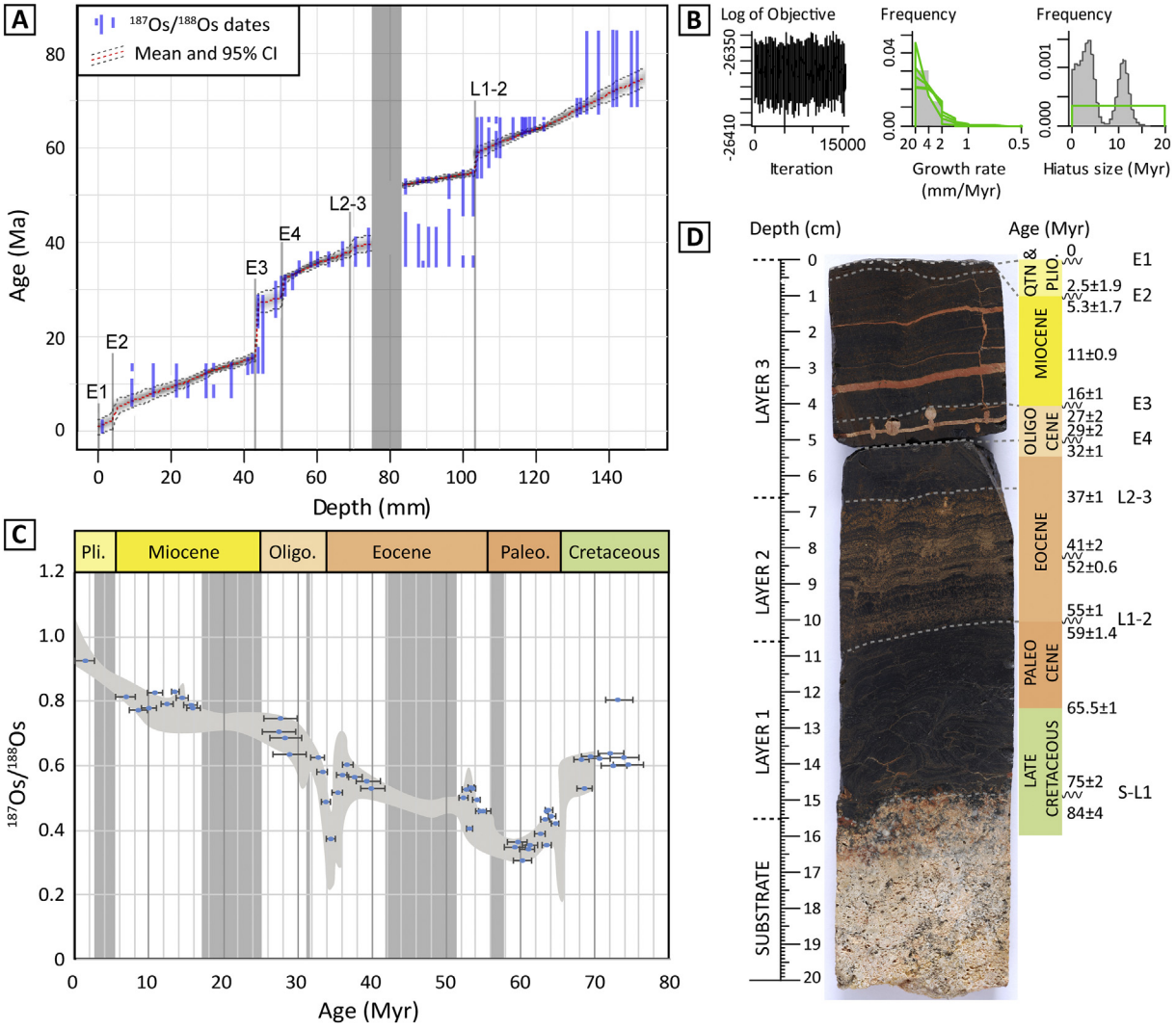

Fig. 6. (A) Age-depth model of core 085_004 overlaying the distribution of valid or passing intervals contained within the Os age envelope (Fig. 5C). The model is presented as shades of grey representing the relative density of MCMC iterations, the dotted line indicates the mean of the model's with 95% probability intervals in dark grey. The position of hiatuses is shown as vertical grey bands. The hiatus around 80 mm is wider due to the absence of visual observation on the core and low Os data density in this depth interval. The panels on (B) depict the MCMC iterations (left; good runs show a stationary distribution with little structure among neighbouring iterations) with prior conditions in green and resulting calculated conditions from the model in grey for the growth rate (middle) and size of potential hiatuses required to adjust the model (right) (Blaauw and Christen, 2011). (C) Distribution of Os isotopes data based on statistical modelling. (D) Visual adaptation of the age model from the statistical modelling to core 085_004 tying together the whole dataset. (For interpretation of the references to colour in this figure legend, the reader is referred to the web version of this article.)

from Co-chronometry remain debatable, the strong correlation observed between our calculations and the growth rate derived from $^{10}Be/^{9}Be$ radiometric dating of a Tropic Seamount sample (Koschinsky et al., 1996), provides confidence in using the growth rates calculated in a composite age model. The composite model is developed using Bayesian statistical modelling of MCMC via the R package "rBacon" (Blaauw and Christen, 2011). Osmium ages retained for the creation of the age envelope are implemented as valid possibilities or 'passing gates' for the simulations. Hiatuses were added into the code to accommodate the model where the slope of the simulation deviated from input values. Coded hiatuses allow the simulation to ignore the influence of neighbouring samples on either side of the boundary. The model was coded to adjust the simulation if required with time gaps at depths of 00, 04, 43, 51, 69 and 103 mm, which match the depth of identified erosive surfaces and boundaries in the core (Fig. 2). Each simulation of the MCMC (4000 per stratigraphic mm), uses a random growth rate taken within a gamma distribution of the Co-chronometer values contained in each stratigraphic interval. These are defined by the potential hiatuses and layer boundaries (Fig. 6A). Consequently, the model calculates and retains as valid possibilities, a series of slopes using Co-chronometer values constrained by the Os isotope 'passing gates'. Simulations not achieving the fit to the Os age intervals are rejected and the resulting successful simulations are compiled into the model presented in Fig. 6. An average with a 95% confidence interval can be calculated using the relative density of MCMC simulation at any given point (Supplementary data 6). The extent of the age envelope defined by Os data is limited by the U-Pb dating of the substrate. The model was run with the envelope constrained at both 80 and 88 Myr. However, this did not produce any change in the resulting model as the growth rate in the lower part of the core prevents the model extending beyond the age of 77 Myr.

The model shows that a minimum of five hiatuses is required to fit the growth rate age model to the Os age intervals from the age envelope (Fig. 6). Out of the six potential discontinuities identified previously, four form statistically representative time-gaps at depths of 04, 43, 51 and 103 mm. The age of the hiatus on the top surface cannot be

accurately estimated due to the lack of a tie point at this end of the model. As a result, the hiatus is accommodated in the large age uncertainty associated with the first sample. The boundary between layers 2 and 3 (L2 − 3) at 69 mm does not produce a major shift in the model suggesting that a statistically significant time gap does not exist at the transition between the two macro layers. In contrast, the transition between layers 1 and 2, marked by a prominent change in texture, represents an important hiatus. Furthermore, the growth rate in macro layer 2 does not permit the model to fit within the defined Os 'passing gates'. Therefore, an important hiatus has to be added, centred around 80 mm depth. Due to the intense phosphatisation of this macro layer, no visible discontinuity can be observed in the Fe-Mn oxide layers and therefore the age model is uncertain between 74 and 84 mm. Below 84 mm, the model is best accommodated by passing through the older potential ages for the Os 'passing gates' between 84 and 103 mm depth, for two reasons: (i) the slope of the model has to be low in this portion of the core as a result of the high growth rate (up to 24 mm/Myr); and (ii) the Os sample at 89 mm, effectively constrains the model to ages of 34.7–36 Myr or 51–52 Myr. As a result, the older (upper) potential ages for each sample offer the best fit for these two conditions.

The model therefore predicts that this Fe-Mn crust commenced growing 73–77 Ma, and indicates a time gap of 2.5–12 Myr between the formation of the carbonate substrate (84 ± 4 Myr) and the initiation of Fe-Mn crust accumulation. This period probably represents the time required for the substrate to subside from just below sea-level, where it formed, to a depth where Fe-Mn crust is stable.

Missing portions of the record occur during the Pliocene (2.5 ± 1.9–5.3 ± 1.7 Ma), Early Miocene (16 ± 1–27 ± 2 Ma), Oligocene (29 ± 2–32 ± 1 Ma), Eocene (41 ± 2–52 ± 0.6 Ma), and Late Paleocene (55 ± 1–59 ± 1.4 Ma). The phosphatisation front (L2–3, 69 mm) affecting the core can be accurately dated to the Late Eocene (38 ± 1.2 Ma).

5. Discussion

5.1. Fe-Mn crusts at Tropic Seamount

Although the U-Pb dating of the carbonate basement for this sample limits the age of the crust to 84 ± 4 Myr, it is possible to envisage that older crusts might be present in other parts of the seamount. As such, the maximum age limit for Fe-Mn deposits at Tropic Seamount is hard to determine accurately and could be anywhere between the age of formation of the seamount, assuming immediate Fe-Mn accumulation on stabilised volcanic flanks, and the age of the carbonate platform dated here.

Considering the 95% confidence interval on the age-depth model, hiatuses in core 085_004 represent between 19 and 47 Myr of time, with the most important hiatuses occurring in the Early Miocene and Middle Eocene. In terms of paleoceanographic reconstructions, interpretation of the significance of these hiatuses and their extent is highly uncertain and potentially more complex to explain than the changes in the core's geochemistry itself. These portions of the Fe-Mn record may have been lost as a result of periods of erosion or chemical dissolution, or simply represent periods when conditions were not conducive to Fe-Mn oxide deposition. More detailed investigation of the morphology of the contacts by scanning electron microscopy (SEM) and other proxies such as high-resolution geochemistry and textural observation may provide new evidence for the causes of these hiatuses. Here, it can be argued that both E1 and E2 represent physical erosive surfaces, based on their cross-cutting morphologies and polishing of the sample surface. Equally, the L1–2 contact presents conformable Fe-Mn layers between two layers with distinct textures, which is indicative of an environment in which Fe-Mn oxides are not being deposited or periods of partial dissolution.

The phosphatised front (L2–3) occurring at a depth of 69 mm can be dated to the Late Eocene, at 38 ± 1.2 Ma. Although multiple phosphatisation episodes may have affected this sample, the age of the phosphatised front represents the most recent episode of CFA impregnation and is within the range of the U-Pb dating of the phosphatised vein (46 ± 10 Ma). This date is consistent with the major phosphatisation episode also identified in Pacific phosphorites and crusts dated by Sr isotopes (39–34 Ma, with a peak at 37 Ma) (Hein et al., 1992). The formation of this phosphatic horizon is widely recognised in Pacific seamounts and now also in Atlantic Fe-Mn crusts. Its formation relates to the global overturn of oceanic circulation during the abrupt transition from the hot and sluggish conditions prevailing in the Cretaceous, Paleocene and early Eocene, to colder and more vigorous current conditions resulting from the onset of the Antarctic Circumpolar Current and formation of the thermohaline deep oceanic circulation (Wright and Miller, 1993).

5.2. Best-practice for ferromanganese crust age models

This data set exemplifies the issues with the reliability of age models that are solely derived from Co-chronometers, and which have been extensively used in the literature for the estimation of Fe-Mn crust growth rates and ages. The model of Puteanus and Halbach (1988) is preferred by Frank et al. (1999) and supported by $^{10}Be/^{9}Be$ data from Co-poor crusts (0.3 wt% < [Co] < 0.6 wt%) from the Atlantic, and also by Klemm et al. (2005) for the calibration of the Os isotope stratigraphy of a Co-rich crust from the Pacific. However, the Co-model of Manheim and Lane-Bostwick (1988) is more widely applied, e.g. by Frank et al. (2002), van de Flierdt et al. (2003), Ren et al. (2007), Canet et al. (2008), Muiños et al. (2008), Banerjee et al. (2010), Hein et al. (2016), Conrad et al. (2017), Hein et al. (2017), Marino et al. (2017) and Marino et al. (2018) for crust samples from continental margins, and the Indian, Atlantic and Arctic Ocean.

Although the model from Manheim and Lane-Bostwick (1988) is justified for studies on samples from the Arctic and continental margins (Canet et al., 2008; Hein et al., 2017), where the Co content is below the threshold concentration of 0.24 wt%, all of the other studies identified above could have used either model. With the exception of when Co is < 0.24 wt%, the rationale for using one model over the other in the absence of cross-validation is unclear. Given the resulting difference in growth rate and derived ages between the two models, it is important to evaluate other independent age proxies to justify the use of a particular model. This issue is highlighted by the age of 76 Myr reported by Marino et al. (2017) for a 90 mm thick crust sample from Tropic Seamount based on the model of Manheim and Lane-Bostwick (1988). Our calculation on sample 085_004 for an equivalent thickness of crust reflects this age, but the model is clearly inconsistent with other age constraints. In contrast, using the Co-chronometer model of Puteanus and Halbach with the data presented here gives a result that is consistent with the $^{10}Be/^{9}Be$ radiometric date of 12.3 Myr (average growth rate of 3 mm/Myr) for a 38 mm thick crust from Tropic Seamount (Koschinsky et al., 1996). In terms of best practice, we strongly recommend that future studies should report ages from both models, with appropriate uncertainty estimates calculated on the basis of geochemical measurement precision (2σ Mn, Fe, Co, P) in the absence of additional cross-validation from other techniques. This is even more important when the validity of the assumptions on which the Co-chronometer models are based are considered. Co-age models generally agree with other proxies, such as magnetostratigraphy and biostratigraphy in sediment cores. However, they consistently yield higher age estimates than radiometric dating and do not match the stratigraphic record in parts of the Early Cenozoic, questioning the assumption of a constant Co flux to the ocean (Kyte et al., 1993). Knowledge from the GEOTRACES program supports this view, as it indicates that Co flux to the seafloor is unlikely to be constant in time and space (Schlitzer et al., 2018). As a result, paleoceanographic reconstruction solely based on Co-chronometry should be avoided, as age estimates are only accurate within their reported uncertainty, which means they only provide a

broad minimal estimate of Fe-Mn crust age.

Further research is still required to validate many of the assumptions used in the dating techniques when they are applied to marine Fe-Mn crusts from different locations, and/or quantify the error associated with these. This may help to reconcile the significant discrepancies observed in the ages derived from different radiometric techniques and allow recalibration of the Co-chronometer models.

6. Conclusions

The results demonstrate the importance of using multiple and independent proxies for the development of age models extending beyond the validity of the ^{230}Th (1 Ma) and ^{10}Be/^{9}Be (10 Ma) methods that have been traditionally used for dating deep-sea Fe-Mn crusts. The evaluation of crust age and growth rate through combined chemostratigraphy, empirical methods, and absolute dating allows for cross-validation of the different methods and statistical modelling reduces uncertainty in the resulting age-depth model. This study has demonstrated the value of this approach by highlighting the widespread bias and discrepancies in pre-existing studies.

The two empirical Co-chronometer models provide significantly different ages for crusts from the Saharan Seamount Province. Cross-validation is essential to determine the closest approximation for the growth rate of the sample considered. Here, the model from Puteanus and Halbach (1988) is preferred based on concordance with ^{10}Be/^{9}Be data (Koschinsky et al., 1996) and a U-Pb absolute date for the carbonate basement.

Bayesian statistical modelling is achieved using Markov Chain Monte Carlo simulations from the rBacon statistical package developed for R©. Using the age of the substrate defined by U-Pb dating, Co-chronometer growth rates and age intervals derived from Os isotopes data, the model combines the proxies to define a composite age-depth relationship with reduced uncertainties compared to using the methods independently.

The results of the composite age models demonstrate that favourable conditions for the formation of hydrogenetic Fe-Mn deposits on Tropic Seamount existed from at least the Late Cretaceous (75 ± 2 Ma). Hiatuses in the stratigraphic record, whether the result of erosion or periods of no Fe-Mn deposition, represent a period of between 19 and 47 Myr, which is split between a minimum of five stratigraphic intervals.

Seamounts are heterogeneous and highly dynamic environments (Lusty et al., 2018). Further studies on samples collected on Tropic Seamount and surrounding seamounts should investigate the continuity of the stratigraphic record, in terms of both the growth periods and the extent of hiatuses, at the local and regional scale. Observations that either validate or disprove the continuity of the preserved records in both space and time at the local scale (meter to kilometre) would greatly inform understanding of the continuity of Fe-Mn deposits across ocean edifices, with implications for mineral exploration and resource evaluation.

Supplementary data to this article can be found online at https://doi.org/10.1016/j.chemgeo.2019.03.003.

Declaration of interest

None.

Acknowledgements

PJ, PL, MH, SC, JR publish with the permission of the Executive Director, British Geological Survey (UKRI). This research was supported by Natural Environmental Research Council (NERC) grants NE/M011186/1 (awarded to B. Murton) and NE/M011151/1 (awarded to P. Lusty), which fund the MarineE-Tech project. We wish to thank the Editor, Dr. B. Peucker-Ehrenbrink, and another anonymous reviewer for their helpful comments to improve this manuscript. The authors gratefully thank the team involved in the RRS James Cook JC142 expedition to Tropic Seamount in 2016. Leanne Staddon is thanked for her help in the laboratory at the University of Bristol, and Christopher Williams, Diana Sahy and Tim Van Peer for their help in discussing the statistical modelling.

References

Abouchami, W., Galer, S.J.G., Koschinsky, A., 1999. Pb and Nd isotopes in NE Atlantic Fe–Mn crusts: proxies for trace metal paleosources and paleocean circulation. Geochim. Cosmochim. Acta 63, 1489–1505.

Banerjee, R., Gupta, S.M., Miura, H., Borole, D.V., 2010. A 400 ka supra-Milankovitch cycle in the Na, Mg, Pb, Ni and Co records of a ferromanganese crust from the Vityaz fracture zone, central Indian ridge. Clim. Past Discuss. 6.

Becker, J.J., Sandwell, D.T., Smith, W.H.F., Braud, J., Binder, B., Depner, J., Fabre, D., Factor, J., Ingalls, S., Kim, S.H., Ladner, R., Marks, K., Nelson, S., Pharaoh, A., Trimmer, R., Von Rosenberg, J., Wallace, G., Weatherall, P., 2009. Global bathymetry and elevation data at 30 arc seconds resolution: SRTM30_PLUS. Mar. Geod. 32, 355–371.

Birck, J.L., Barman, M.R., Capmas, F., 1997. Re-Os isotopic measurements at the femtomole level in natural samples. Geostand. Newslett. 21, 19–27.

Blaauw, M., Christen, J.A., 2011. Flexible paleoclimate age-depth models using an autoregressive gamma process. Bayesian Anal. 6, 457–474.

Blum, N., Halbach, P., Münch, U., 1996. Geochemistry and mineralogy of alkali basalts from Tropic Seamount, Central Atlantic Ocean. Mar. Geol. 136, 1–19.

Burton, K.W., Bourdon, B., Birck, J.L., Allègre, C., Hein, J.R., 1999. Osmium isotope variations in the oceans recorded by FeMn crusts. Earth Planet. Sci. Lett. 171 (1), 185–197.

Canet, C., Prol-Ledesma, R.M., Bandy, W.L., Schaaf, P., Linares, C., Camprubí, A., Tauler, E., Mortera-Gutiérrez, C., 2008. Mineralogical and geochemical constraints on the origin of ferromanganese crusts from the Rivera plate (western margin of Mexico). Mar. Geol. 251, 47–59.

Christensen, J.N., Halliday, A.N., Godfrey, L.V., Hein, J.R., Rea, D.K., 1997. Climate and ocean dynamics and the lead isotopic records in Pacific ferromanganese crusts. Science 277, 913–918.

Claude, C., Suhr, G., Hofmann, A.W., Koschinsky, A., 2005. U-Th chronology and paleoceanographic record in a Fe-Mn crust from the NE Atlantic over the last 700 ka. Geochim. Cosmochim. Acta 69, 4845–4854.

Cohen, A.S., Waters, F.G., 1996. Separation of osmium from geological materials by solvent extraction for analysis by thermal ionisation mass spectrometry. Anal. Chim. Acta 332, 269–275.

Conrad, T., Hein, J.R., Paytan, A., Clague, D.A., 2017. Formation of Fe-Mn crusts within a continental margin environment. Ore Geol. Rev. 87, 25–40.

David, K., Frank, M., O'Nions, R.K., Belshaw, N.S., Arden, J.W., 2001. The Hf isotope composition of global seawater and the evolution of Hf isotopes in the deep Pacific Ocean from Fe–Mn crusts. Chem. Geol. 178, 23–42.

Frank, M., O'Nions, R.K., 1998. Sources of Pb for Indian Ocean ferromanganese crusts: a record of Himalayan erosion? Earth Planet. Sci. Lett. 158, 121–130.

Frank, M., O'Nions, R.K., Hein, J.R., Banakar, V.k., 1999. 60 Myr records of major elements and Pb-Nd isotopes from hydrogenous ferromanganese crusts: Reconstruction of seawater paleochemistry. Geochim. Cosmochim. Acta 63, 1689–1708.

Frank M., Whiteley N., Kasten S., Hein J.R. and O'Nions K. (2002) North Atlantic Deep Water export to the Southern Ocean over the past 14 Myr: evidence from Nd and Pb isotopes in ferromanganese crusts. Paleoceanography 17, 12-11-12-19.

Futa, K., Peterman, Z.E., Hein, J.R., 1988. Sr and Nd isotopic variations in ferromanganese crusts from the Central Pacific - implications for age and source provenance. Geochim. Cosmochim. Acta 52, 2229–2233.

Goto, K.T., Anbar, A.D., Gordon, G.W., Romaniello, S.J., Shimoda, G., Takaya, Y., Tokumaru, A., Nozaki, T., Suzuki, K., Machida, S., Hanyu, T., Usui, A., 2014. Uranium isotope systematics of ferromanganese crusts in the Pacific Ocean: implications for the marine 238U/235U isotope system. Geochim. Cosmochim. Acta 146, 43–58.

Halbach, P., Segl, M., Puteanus, D., Mangini, A., 1983. Co-fluxes and growth rates in ferromanganese deposits from central Pacific seamount areas. Nature 304, 716.

Hein, J.R., Bohrson, W.A., Schulz, M.S., Noble, M., Clague, D.A., 1992. Variations in the fine-scale composition of a central Pacific ferromanganese crust: paleoceanographic implications. Paleoceanography 7, 63–77.

Hein, J.R., Koschinsky, A., Bau, M., Manheim, F.T., Kang, J.-K., Roberts, L., 2000. Cobalt-rich ferromanganese crusts in the Pacific. In: Cronan, D.S. (Ed.), Handbook of Marine Minerals Deposit. CRC Press, Boca Raton, Florida, pp. 239–279.

Hein, J.R., Conrad, T., Mizell, K., Banakar, V.K., Frey, F.A., Sager, W.W., 2016. Controls on ferromanganese crust composition and reconnaissance resource potential, Ninetyeast Ridge, Indian Ocean. Deep-Sea Res. I Oceanogr. Res. Pap. 110, 1–19.

Hein, J.R., Konstantinova, N., Mikesell, M., Mizell, K., Fitzsimmons, J.N., Lam, P.J., Jensen, L.T., Xiang, Y., Gartman, A., Cherkashov, G., Hutchinson, D.R., Till, C.P., 2017. Arctic deep water ferromanganese-oxide deposits reflect the unique characteristics of the Arctic Ocean. Geochem. Geophys. Geosyst. 18, 3771–3800.

Henderson, G.M., Burton, K.W., 1999. Using (234U/238U) to assess diffusion rates of isotope tracers in ferromanganese crusts. Earth Planet. Sci. Lett. 170, 169–179.

Hu, R., Chen, T., Ling, H., 2012. Late Cenozoic history of deep water circulation in the western North Pacific: evidence from Nd isotopes of ferromanganese crusts. Chin. Sci. Bull. 57, 4077–4086.

Ingram, B.L., Hein, J.R., Farmer, G.L., 1990. Age-determinations and growth-rates of Pacific ferromanganese deposits using strontium isotopes. Geochim. Cosmochim. Acta 54, 1709–1721.
Joshima, M., Usui, A., 1998. Magnetostratigraphy of hydrogenetic manganese crusts from northwestern Pacific seamounts. Mar. Geol. 146, 53–62.
Josso, P., Pelleter, E., Pourret, O., Fouquet, Y., Etoubleau, J., Cheron, S., Bollinger, C., 2017. A new discrimination scheme for oceanic ferromanganese deposits using high field strength and rare earth elements. Ore Geol. Rev. 87, 3–15.
Klemm, V., Levasseur, S., Frank, M., Hein, J.R., Halliday, A.N., 2005. Osmium isotope stratigraphy of a marine ferromanganese crust. Earth Planet. Sci. Lett. 238, 42–48.
Koschinsky, A., Halbach, P., 1995. Sequential leaching of marine ferromanganese precipitates: genetic implications. Geochim. Cosmochim. Acta 59, 5113–5132.
Koschinsky, A., Hein, J.R., 2003. Uptake of elements from seawater by ferromanganese crusts: solid-phase associations and seawater speciation. Mar. Geol. 198, 331–351.
Koschinsky, A., Hein, J.R., 2017. Marine ferromanganese encrustations: archives of changing oceans. Elements 13 (3), 177–182.
Koschinsky, A., Halbach, P., Hein, J.R., Mangini, A., 1996. Ferromanganese crusts as indicators for paleoceanographic events in the NE Atlantic. Geol. Rundsch. 85, 567–576.
Koschinsky, A., Stascheit, A., Bau, M., Halbach, P., 1997. Effects of phosphatization on the geochemical and mineralogical composition of marine ferromanganese crusts. Geochim. Cosmochim. Acta 61, 4079–4094.
Kyte, F.T., Leinen, M., Ross, Heath G., Zhou, L., 1993. Cenozoic sedimentation history of the central North Pacific: Inferences from the elemental geochemistry of core LL44-GPC3. Geochim. Cosmochim. Acta 57, 1719–1740.
Lee, D.-C., Halliday, A.N., Hein, J.R., Burton, K.W., Christensen, J.N., Günther, D., 1999. Hafnium isotope stratigraphy of ferromanganese crusts. Science 285, 1052–1054.
Ling, H.F., Burton, K.W., O'Nions, R.K., Kamber, B.S., von Blanckenburg, F., Gibb, A.J., Hein, J.R., 1997. Evolution of Nd and Pb isotopes in central Pacific seawater from ferromanganese crusts. Earth Planet. Sci. Lett. 146, 1–12.
Ling, H.-F., Jiang, S.-Y., Frank, M., Zhou, H.-Y., Zhou, F., Lu, Z.-L., Chen, X.-M., Jiang, Y.-H., Ge, C.-D., 2005. Differing controls over the Cenozoic Pb and Nd isotope evolution of deepwater in the central north Pacific ocean. Earth Planet. Sci. Lett. 232, 345–361.
Ludwig K.R. (2012) Users manual for isoplot 3.75 A geochronological toolkit for Microsoft Excel. Berkeley Geochronology Center Special Publication No.5.
Lusty, P., Hein, J.R., Josso, P., 2018. Formation and occurrence of ferromanganese crusts: earth's storehouse for critical metals. Elements 14, 313–318.
Manheim, F.T., Lane-Bostwick, C.M., 1988. Cobalt in ferromanganese crusts as a monitor of hydrothermal discharge on the Pacific sea floor. Nature 335, 59–62.
Marino, E., González, F.J., Somoza, L., Lunar, R., Ortega, L., Vázquez, J.T., Reyes, J., Bellido, E., 2017. Strategic and rare elements in Cretaceous-Cenozoic cobalt-rich ferromanganese crusts from seamounts in the Canary Island Seamount province (northeastern tropical Atlantic). Ore Geol. Rev. 87, 41–61.
Marino, E., González, F., Lunar, R., Reyes, J., Medialdea, T., Castillo-Carrión, M., Bellido, E., Somoza, L., 2018. High-resolution analysis of critical minerals and elements in Fe–Mn crusts from the Canary Island Seamount province (Atlantic ocean). Minerals 8, 285.
McDowell, F.W., McIntosh, W.C., Ball, L., 2009. A precise 40Ar-39Ar reference age for the Durango apatite (U-Th)/He and fission-track dating standard. Chem. Geol. 214, 3–4.
Miller, C.A., Peucker-Ehrenbrink, B., Ball, L., 2009. Precise determination of rhenium isotope composition by multi-collector inductively-coupled plasma mass spectrometry. J. Anal. At. Spectrom. 24, 1069–1078.
Muiños S.B., Frank M., Maden C., Hein J.R., van de Flierdt T., Lebreiro S.M., Gaspar L., Monteiro J.H. and Halliday A.N. (2008) New constraints on the Pb and Nd isotopic evolution of NE Atlantic water masses. Geochem. Geophys. Geosyst. 9, n/a-n/a.
Nielsen, S.G., Mar-Gerrison, S., Gannoun, A., LaRowe, D., Klemm, V., Halliday, A.N., Burton, K.W., Hein, J.R., 2009. Thallium isotope evidence for a permanent increase in marine organic carbon export in the early Eocene. Earth Planet. Sci. Lett. 278, 297–307.
Noguchi, A., Yamamoto, Y., Nishi, K., Usui, A., Oda, H., 2017. Paleomagnetic study of ferromanganese crusts recovered from the northwest Pacific — testing the applicability of the magnetostratigraphic method to estimate growth rate. Ore Geol. Rev. 87, 16–24.
Oda, H., Usui, A., Miyagi, I., Joshima, M., Weiss, B.P., Shantz, C., Fong, L.E., McBride, K.K., Harder, R., Baudenbacher, F.J., 2011. Ultrafine-scale magnetostratigraphy of marine ferromanganese crust. Geology 39, 227–230.
Oda, H., Kawai, J., Miyamoto, M., Miyagi, I., Sato, M., Noguchi, A., Yamamoto, Y., Fujihira, J.I., Natsuhara, N., Aramaki, Y., Masuda, T., Xuan, C., 2016. Scanning SQUID microscope system for geological samples: system integration and initial evaluation. Earth Planets Space 68 (19p).
Palomino, D., Vázquez, J.-T., Somoza, L., León, R., López-González, N., Medialdea, T., Fernández-Salas, L.-M., González, F.-J., Rengel, J.A., 2016. Geomorphological features in the southern Canary Island volcanic province: the importance of volcanic processes and massive slope instabilities associated with seamounts. Geomorphology 255, 125–139.
Patriat, M., Labails, C., 2006. Linking the Canary and Cape-Verde hot-spots, northwest Africa. Mar. Geophys. Res. 27, 201–215.
Pegram, W.J., Turekian, K.K., 1999. The osmium isotopic composition change of Cenozoic Sea water as inferred from a deep-sea core corrected for meteoritic contributions. Geochim. Cosmochim. Acta 63, 4053–4058.
Peucker-Ehrenbrink, B., Ravizza, G., 2012. Chapter 8 - Osmium Isotope Stratigraphy, The Geologic Time Scale. Elsevier, Boston, pp. 145–166.
Puteanus, D., Halbach, P., 1988. Correlation of Co concentration and growth rate - a method for age determination of ferromanganese crusts. Chem. Geol. 69, 73–85.
Ravizza, G., Peucker-Ehrenbrink, B., 2003. The marine 187Os/188Os record of the Eocene–Oligocene transition: the interplay of weathering and glaciation. Earth Planet. Sci. Lett. 210, 151–165.
Ren, X., Glasby, G.P., Liu, J., Shi, X., Yin, J., 2007. Fine-scale compositional variations in a Co-rich Mn crust from the Marcus-Wake Seamount cluster in the western Pacific based on electron microprobe analysis (EMPA). Mar. Geophys. Res. 28, 165–182.
Reusch, D.N., Ravizza, G., Maasch, K.A., Wright, J.D., 1998. Miocene seawater 187Os/188Os ratios inferred from metalliferous carbonates. Earth Planet. Sci. Lett. 160, 163–178.
Reynolds, B.C., Frank, M., O'Nions, R.K., 1999. Nd- and Pb-isotope time series from Atlantic ferromanganese crusts: implications for changes in provenance and paleocirculation over the last 8 Myr. Earth Planet. Sci. Lett. 173, 381–396.
Roberts, N.M.W., Rasbury, E.T., Parrish, R.R., Smith, C.J., Horstwood, M.S.A., Condon, D.J., 2017. A calcite reference material for LA-ICP-MS U-Pb geochronology. Geochem. Geophys. Geosyst. 18, 2807–2814.
Schlitzer, R., Anderson, R.F., Dodas, E.M., Lohan, M., Geibert, W., Tagliabue, A., Bowie, A., Jeandel, C., Maldonado, M.T., Landing, W.M., Cockwell, D., Abadie, C., Abouchami, W., Achterberg, E.P., Agather, A., Aguliar-Islas, A., van Aken, H.M., Andersen, M., Archer, C., Auro, M., de Baar, H.J., Baars, O., Baker, A.R., Bakker, K., Basak, C., Baskaran, M., Bates, N.R., Bauch, D., van Beek, P., Behrens, M.K., Black, E., Bluhm, K., Bopp, L., Bouman, H., Bowman, K., Bown, J., Boyd, P., Boye, M., Boyle, E.A., Branellec, P., Bridgestock, L., Brissebrat, G., Browning, T., Bruland, K.W., Brumsack, H.-J., Brzezinski, M., Buck, C.S., Buck, K.N., Buesseler, K., Bull, A., Butler, E., Cai, P., Mor, P.C., Cardinal, D., Carlson, C., Carrasco, G., Casacuberta, N., Casciotti, K.L., Castrillejo, M., Chamizo, E., Chance, R., Charette, M.A., Chaves, J.E., Cheng, H., Chever, F., Christl, M., Church, T.M., Closset, I., Colman, A., Conway, T.M., Cossa, D., Croot, P., Cullen, J.T., Cutter, G.A., Daniels, C., Dehairs, F., Deng, F., Dieu, H.T., Duggan, B., Dulaquais, G., Dumousseaud, C., Echegoyen-Sanz, Y., Edwards, R.L., Ellwood, M., Fahrbach, E., Fitzsimmons, J.N., Russell, Flegal A., Fleisher, M.Q., van de Flierdt, T., Frank, M., Friedrich, J., Fripiat, F., Fröllje, H., Galer, S.J.G., Gamo, T., Ganeshram, R.S., Garcia-Orellana, J., Garcia-Solsona, E., Gault-Ringold, M., George, E., Gerringa, L.J.A., Gilbert, M., Godoy, J.M., Goldstein, S.L., Gonzalez, S.R., Grissom, K., Hammerschmidt, C., Hartman, A., Hassler, C.S., Hathorne, E.C., Hatta, M., Hawco, N., Hayes, C.T., Heimbürger, L.-E., Helgoe, J., Heller, M., Henderson, G.M., Henderson, P.B., van Heuven, S., Ho, P., Horner, T.J., Hsieh, Y.-T., Huang, K.-F., Humphreys, M.P., Isshiki, K., Jacquot, J.E., Janssen, D.J., Jenkins, W.J., John, S., Jones, E.M., Jones, J.L., Kadko, D.C., Kayser, R., Kenna, T.C., Khondoker, R., Kim, T., Kipp, L., Klar, J.K., Klunder, M., Kretschmer, S., Kumamoto, Y., Laan, P., Labatut, M., Lacan, F., Lam, P.J., Lambelet, M., Lamborg, C.H., Le Moigne, F.A.C., Le Roy, E., Lechtenfeld, O.J., Lee, J.-M., Lherminier, P., Little, S., López-Lora, M., Lu, Y., Masque, P., Mawji, E., McClain, C.R., Measures, C., Mehic, S., Barraqueta, J.-L.M., van der Merwe, P., Middag, R., Mieruch, S., Milne, A., Minami, T., Moffett, J.W., Moncoiffe, G., Moore, W.S., Morris, P.J., Morton, P.L., Nakaguchi, Y., Nakayama, N., Niedermiller, J., Nishioka, J., Nishiuchi, A., Noble, A., Obata, H., Ober, S., Ohnemus, D.C., van Ooijen, J., O'Sullivan, J., Owens, S., Pahnke, K., Paul, M., Pavia, F., Pena, L.D., Peters, B., Planchon, F., Planquette, H., Pradoux, C., Puigcorbé, V., Quay, P., Queroue, F., Radic, A., Rauschenberg, S., Rehkämper, M., Rember, R., Remenyi, T., Resing, J.A., Rickli, J., Rigaud, S., Rijkenberg, M.J.A., Rintoul, S., Robinson, L.F., Roca-Martí, M., Rodellas, V., Roeske, T., Rolison, J.M., Rosenberg, M., Roshan, S., Rutgers van der Loeff, M.M., Ryabenko, E., Saito, M.A., Salt, L.A., Sanial, V., Sarthou, G., Schallenberg, C., Schauer, U., Scher, H., Schlosser, C., Schnetger, B., Scott, P., Sedwick, P.N., Semiletov, I., Shelley, R., Sherrell, R.M., Shiller, A.M., Sigman, D.M., Singh, S.K., Slagter, H.A., Slater, E., Smethie, W.M., Snaith, H., Sohrin, Y., Sohst, B., Sonke, J.E., Speich, S., Steinfeldt, R., Stewart, G., Stichel, T., Stirling, C.H., Stutsman, J., Swarr, G.J., Swift, J.H., Thomas, A., Thorne, K., Till, C.P., Till, R., Townsend, A.T., Townsend, E., Tuerena, R., Twining, B.S., Vance, D., Velazquez, S., Venchiarutti, C., Villa-Alfageme, M., Vivancos, S.M., Voelker, A.H.L., Wake, B., Warner, M.J., Watson, R., van Weerlee, E., Alexandra, Weigand M., Weinstein, Y., Weiss, D., Wisotzki, A., Woodward, E.M.S., Wu, J., Wu, Y., Wuttig, K., Wyatt, N., Xiang, Y., Xie, R.C., Xue, Z., Yoshikawa, H., Zhang, J., Zhang, P., Zhao, Y., Zheng, L., Zheng, X.-Y., Zieringer, M., Zimmer, L.A., Ziveri, P., Zunino, P., Zurbrick, C., 2018. The GEOTRACES Intermediate Data Product 2017. Chem. Geol. 493, 210–223.
Schmincke H.U. and Graf C. (2000) DECOS/OMEX II, Cruise No. 43, 25 November 1998–14 January 1999, METEOR-Berichte, Universität Hamburg. 00–2, 99p.
Shirey, S.B., Walker, R.J., 1995. Carius tube digestion for low-blank rhenium-osmium analysis. Anal. Chem. 67, 2136–2141.
Templeton, A.S., Knowles, E.J., Eldridge, D.L., Arey, B.W., Dohnalkova, A.C., Webb, S.M., Bailey, B.E., Tebo, B.M., Staudigel, H., 2009. A seafloor microbial biome hosted within incipient ferromanganese crusts. Nat. Geosci. 2, 872.
van de Flierdt, T., Frank, M., Halliday, A.N., Hein, J.R., Hattendorf, B., Günther, D., Kubik, P.W., 2003. Lead isotopes in North Pacific deep water – implications for past changes in input sources and circulation patterns. Earth Planet. Sci. Lett. 209, 149–164.
van den Bogaard, P., 2013. The origin of the Canary Island Seamount province - new ages of old seamounts. Sci. Rep. 3, 1–7p.
Vonderhar, D.L., Mahoney, J.J., McMurty, G.M., 1995. An evaluation of strontium isotopic dating of ferromanganese oxides in a marine hydrogenous ferromanganese crust. Geochim. Cosmochim. Acta 59, 4267–4277.
Wang, X., Müller, W.E.G., 2009. Marine biominerals: perspectives and challenges for polymetallic nodules and crusts. Trends Biotechnol. 27, 375–383.
Wright, J.D., Miller, K.G., 1993. Southern Ocean influences on late Eocene to Miocene deep water circulation. In: Kennet, J.P., Warnke, D.A. (Eds.), The Antarctic Paleoenvironment. A Perspective on Global Change. Antarctic Research Series, vol. 60. pp. 1–25.
Yeo, I., Dobson, K., Josso, P., Pearce, R., Howarth, S., Lusty, P., Le Bas, T., Murton, B., 2018. Assessment of the mineral resource potential of Atlantic ferromanganese crusts based on their growth history, microstructure, and texture. Minerals 8, 327.